Raghavendra, A., P. E. Roundy, and L. Zhou, 2019: Trends in Tropical Wave Activity from the 1980s to 2016. *Seventh Symposium on the Madden-Julian Oscillation and Sub-Seasonal Monsoon Variability,* Phoenix, AZ, Amer. Meteor. Soc., 297, https://ams.confex.com/ams/2019Annual/meetingapp.cgi/Paper/350629

3.3A TRENDS IN TROPICAL WAVE ACTIVITY FROM 1980s–2016

Ajay Raghavendra*, Paul E. Roundy, and Liming Zhou
University at Albany, State University of New York, Albany, NY, USA

ABSTRACT

A frequency–wavenumber power (**P**) spectrum was constructed using satellite derived outgoing longwave radiation (OLR), and brightness temperature for the tropical latitudes. Since the two datasets overlap for over 34 years with non-intersecting sources in error and compare relatively well with each other, it is possible to diagnose trends in the tropical wave activity from the two datasets with confidence. The results suggest a weakening trend in **P** characterized by high interannual variability for wave activity occurring in the low frequency part of the spectrum, and a steady increase in **P** with relatively low interannual variability for wave activity occurring in the high frequency part of the spectrum. The results show the parts of the spectrum representing the Madden–Julian oscillation and equatorial Rossby wave losing **P**, and other parts of the spectrum representing Kelvin waves, mixed Rossby gravity waves, and tropical disturbance like wave activity gaining **P**. Similar results were obtained when trends in variance corresponding to the first principle component was produced using spectrally filtered OLR data representative of atmospheric equatorial waves. Spatial trends in the active phase of wave events, and the mean duration of events are shown for the different wave types. Linear trends in **P** for the entire spectrum, and regional means in the spectrum corresponding to the abovementioned five wave types with confidence intervals are also presented in the paper. Finally, we demonstrate that El Niño–Southern Oscillation variability does not appear to control the overall spatial patterns and trends observed in the **P** spectrum.

Key words: Frequency–wavenumber power spectrum, outgoing longwave radiation, satellite IR brightness temperature, tropical climate change and trends, and tropical waves.

1. Introduction

Holton and Hakim (2013) elegantly stated the necessity to study the tropics separately from the mid-latitudes given the complexity of dynamics making up the tropical circulation. Unlike the mid-latitudes that are mostly dominated by Rossby wave dynamics, the tropical latitudes house many different disturbances such as equatorial Rossby (ER) waves, Kelvin waves, mixed Rossby gravity (MRG) waves, Madden–Julian oscillation (MJO; Madden and Julian 1971, 1972), and tropical depression-type disturbances (TDs). Furthermore, the mid-latitude dynamics are relatively better understood and explained by using models such as the quasi geostrophic framework, but a similar parallel and concise dynamic–thermodynamic framework to understand tropical dynamics does not exist yet. Since these waves are strongly linked to the dynamics observed in the Earth's atmosphere, understanding how these waves may have/continue to change will help us better understand atmospheric convection, precipitation characteristics, and energy redistribution. From the standpoint of climate change and variability, it is also critical to improve our understanding and prediction of the change of the Earth's climate system. For instance, some studies have explored changes and long-term trends in the inter-tropical convergence zone (ITCZ) using observations and modeling experiments and have concluded that the ITCZ may be intensifying and narrowing in a warming climate (e.g., Byrne and Schneider 2016). If this is true, the ITCZ may more readily breakdown and result in an increased occurrence of tropical disturbances (e.g., Raghavendra and Guinn 2016). As an illustration, Fig. 1c shows the long-term changes in deseasonalized outgoing longwave radiation (OLR) anomalies from 1979–2016 where we observe an intensification and shift in convection over the northern tropical latitudes and vice-versa. There is also a slight preference for convection consistent with a La Niña-like state in Fig. 1b–c since we have experienced increased occurrence of La Niña in recent years (e.g., Cai et al. 2015).

While the behavior and anticipated changes of mid-latitude waves are well captured and documented with relatively high confidence using climate models (e.g., Francis and Vavrus 2012), a similar analysis is difficult and therefore lacking over the tropics. In fact, very few global climate models (GCMs) used in the Coupled Model Intercomparison Project (CMIP) phase 5 (CMIP5) were able to simulate what metrics such as the frequency(f)-wavenumber (k) power (**P**) spectrum (Wheeler and Kaladis 1999 hereafter WK99) suggest is a realistic MJO (Hung et al. 2013). Unfortunately, today's weather and climate models (e.g., Hung et al. 2013; Schiraldi and Roundy 2017) struggle to accurately resolve these waves for many reasons. These limitations seen in models may be attributed to coarse resolution and poor parameterization of moist processes, and the different and complex spatiotemporal structures of waves observed near the equator that are often ill-resolved by GCMs. Many studies have tried to understand changes in the tropical ocean (e.g., Rose et al. 2014), land surface (e.g., Zhou

* *Corresponding author address:* Ajay Raghavendra, Dept. of Atmospheric and Environmental Sciences, University at Albany, 1400 Washington Ave., Albany, NY–12222; e-mail: araghavendra@albany.edu

et al. 2014), and atmosphere (e.g., Hua et al. 2016; 2018) using observations, reanalyses, and regional/global models. These studies have proven imperative to improving our understanding of the role of the tropical latitudes in redistributing energy, momentum, and moisture across the globe, and regulating the Earth's climate (e.g., Trenberth and Stepaniak 2004; Lewis 2006).

Since GCMs are generally unreliable to diagnose tropical waves in both the historic runs and possible future climate scenarios (Hung et al. 2013), long-term observations and reanalysis datasets are the best sources to capture possible effects of climate change and variability notwithstanding dataset uncertainties and caveats (e.g., Santer et al. 2003). Considering the paramount importance of the role of tropical waves and convection on global weather and climate (e.g., Lin et al. 2006), understanding long-term changes in tropical wave activity may provide valuable insight to better estimating the impacts of climate change over tropical latitudes, and global weather and climate patterns.

While numerous studies have investigated tropical waves across different timescales (e.g., Roundy and Frank 2004; Chen and Huang 2009; Huang and Huang 2011; Hung et al. 2013), this paper is motivated by incomplete understanding of climate variability and change in tropical wave activity, and for the first-time sheds light on this glaring issue through the analysis of two long-term satellite based OLR and brightness temperature (T_b) gridded datasets. The datasets were used to document changes and trends in the f-k **P** spectrum over tropical latitudes (i.e., 15°N–15°S). The paper is organized as follows. *Sections 2* and *3* provide a brief description of datasets and methods used. Results pertaining to the long-term trends in **P** spectrum are presented in *section 4*. Major conclusions and possible physical mechanisms are discussed in *section 5*.

2. Satellite Data

Two different (i.e., geostationary and polar orbiting) satellite datasets were used in this study. The gridded infrared (IR) channel brightness temperature T_b dataset (GridSat-B1; Knapp, 2008; Knapp et al. 2011) was produced from geostationary satellite data for 1982–2016 (35 years) from the International Satellite Cloud Climatology Project (ISCCP; Schiffer and Rossow 1983) and was re-mapped on a 0.07-degree latitude equal-angle grid at a 3-hour temporal resolution. In order to meet the need for observational climate studies, much effort has been done to reduce intersatellite differences by rigorous intersatellite calibration and temporal normalization in the GridSat dataset (Knapp et al. 2011). A view zenith angle correction (Joyce et al. 2001) was also applied in producing this dataset. Out of the three channels available in the GridSat-B1 dataset (i.e., visible $0.7\mu m$, IR $11.0\mu m$, and water vapor $7.7\mu m$), only the IR window channel data was used since the other channels did not satisfy the Climate Data Record (CDR) program quality (NRC, 2004). In order to speed-up the mathematical operations and statistical analysis, the 0.07-degree dataset was re-gridded and up scaled to 0.98-degree. The popular and relatively coarser resolution interpolated OLR dataset (Liebmann and Smith 1996) by the National Oceanic and Atmospheric Administration (NOAA) from 1979–2016 (38 years) was also used in this study. The OLR dataset has a temporal resolution of 1-day, a horizontal resolution of $2.5° \times 2.5°$, and was produced using data obtained from polar orbiting satellites. Missing data in both datasets were treated with the gap filling algorithm developed by Garcia (2010) and Wang et al. (2012) that works particularly well for satellite derived datasets. In both datasets, the lower thresholds can be used to detect clouds and quantify cloud top temperatures (Schmetz et al. 1997). The negative OLR and T_b anomalies are often used as a proxy to identify and detect tropical convection (e.g., Raghavendra et al. 2018a). While the OLR dataset has been used in numerous studies to understand convection and dynamics in the tropics (e.g., WK99; Roundy 2018), only few papers have performed similar analyses using T_b data (e.g., Wang and Chen 2016; Wang and Li 2017).

Long-term satellite derived datasets have been widely used to detect and quantify climatic signals in many studies, particularly over the vast and inadequately observed tropical rainforests (e.g., Congo by Zhou et al. 2014; Raghavendra et al. 2018a; Jiang et al. 2018), landmasses such as the Sahara Desert (Wei et al. 2017) and Eurasia (Li et al. 2017), and the oceans (e.g., Barton 1995). However, despite large efforts made to minimize the intersatellite differences in the long-term satellite datasets as mentioned previously, trends established using these datasets are still prone to residual uncertainties and a tropic of considerable debate in the climate community (Santer et al. 2003). Often, the data record is relatively short and limited to the life span of a satellite or scientific mission, and long-term records such as the ones used in this paper were created from multiple satellites and thus may contain non-climate biases and uncertainties (e.g., instrument calibration errors due to satellite drift/changover). In our case, the OLR dataset is constructed using NOAA operated polar orbiting satellites (Liebmann and Smith 1996), and the T_b dataset relies on geostationary satellites deployed by multiple countries (Knapp et al. 2011). Since the two datasets use different types of satellites/sensors and are processed differently, they would be associated with non-intersecting sources of error and uncertainties between them. Here we include both datasets to study long-term changes and trends in tropical wave activity, which can enhance the confidence in our findings and may identify their differences (e.g., Raghavendra et al. 2018a). Although there are only two datasets applied here, they are constructed from numerous satellites. While individual satellites may be associated with systematic trends over short-term periods due to orbital

decay and other factors, these would affect the two datasets differently and would not likely produce monotonic long-term trends over time.

3. Methods

After treating the OLR and T_b for missing data and subsetting to include only the tropical latitudes (i.e., 15°N–15°S), the refined datasets were deseasonalized to prevent aliasing (WK99) using five pairs of harmonics to the annual cycle ($\mathbf{X}$; Roundy 2017). The regression coefficients ($\mathbf{C}$) are given by Eq. 1

$$\mathbf{C} = (\mathbf{X^T} \times \mathbf{X})^{-1} \times \mathbf{X^T} \times \mathbf{Y} \quad \text{(Eq. 1)}$$

where $\mathbf{Y}$ is the 3D (i.e., $time$, lat, and lon) matrix containing OLR or T_b data. Using Eq. 1, the seasonal cycle ($\mathbf{X} \times \mathbf{C}$) was calculated and later subtracted from $\mathbf{Y}$ to obtain the anomalies with respect to $\mathbf{Y}$ (i.e., $\mathbf{Y}_{anom}$). Using techniques similar to WK99, the symmetric ($\mathbf{Y_{symm}}$) and antisymmetric ($\mathbf{Y_{asym}}$) components of the dataset were then computed (Eq 2–3).

$$\mathbf{Y_{symm}} = \frac{\mathbf{Y_{anom}}_{(15°N-0°)} + \mathbf{Y_{anom}}_{(15°S-0°)}}{2} \quad \text{(Eq. 2)}$$

$$\mathbf{Y_{asym}} = \frac{\mathbf{Y_{anom}}_{(15°N-0°)} - \mathbf{Y_{anom}}_{(15°S-0°)}}{2} \quad \text{(Eq. 3)}$$

The $\mathbf{Y_{symm}}$ and $\mathbf{Y_{asym}}$ were subjected to segmentation using 200-day time windows that were detrended and tapered to zero along the ends of the time dimension using a $cosine\ bell$ in order to prevent spectral leakage (WK99). The 200-day windows were repeated along the data array every 100 days. A 200-day window was chosen to increase the number of f bins and resolve the time scales of the motions of interest in this paper. The discrete Fourier transform (DFT) using a fast Fourier transform (FFT; Frigo and Johnson 2005, 1998) was then applied to each 200-day time window, and an FFT shift was applied to rearrange the zero-f component to the middle of the domain iteratively to obtain $FFT(\mathbf{Y_{symm}})$ and $FFT(\mathbf{Y_{asym}})$. Finally, the symmetric and antisymmetric $\mathbf{P}$ was calculated by taking the complex conjugate (i.e., $\mathbf{P_{symm}} = FFT(\mathbf{Y_{symm}}) \times conj[FFT(\mathbf{Y_{symm}})]$ and $\mathbf{P_{asym}} = FFT(\mathbf{Y_{asym}}) \times conj[FFT(\mathbf{Y_{asym}})]$). Similar to WK99, the mean time–latitude $\mathbf{P}$ spectrum for the symmetric and antisymmetric parts was obtained by divided by the smoothened mean background spectrum (i.e., $\frac{\mathbf{P_{symm}}+\mathbf{P_{asym}}}{2}$; see Fig. 2 for normalized $\mathbf{P}$ spectrum). Note that normalization by the background is not necessary for this analysis and since the background is constant it does not impact the trends.

To demonstrate whether the trends in wave activity are consistent with trends in spectral variance corresponding to each wave band, an empirical orthogonal function (EOF) analysis (e.g., Kiladis et al. 2009) was applied to the filtered daily OLR anomaly data from 1979–2016 for the five different wave bands. Trends in signals projecting onto these patterns will correspond to trends conforming to the target EOF modes themselves instead of the background "noise". This analysis was performed by first spectrally filtering the daily long-term OLR dataset to retain only those frequencies and wavelengths representative of the target wave. The spectral filters applied are similar to the spectral bands illustrated in Fig. 2. A data matrix including the entire time series of filtered OLR data on the full tropical grid from 15°N to 15°S was created, and the eigenvectors of the covariance matrix were computed. Only the leading EOF (EOF-1), which explains the largest variance was retained. The filtered data were then projected onto EOF-1 to obtain the timeseries corresponding to the first principle component (PC-1). Variance was obtained by squaring the PC-1 timeseries. A trend in variance was obtained by using linear regression, with time as the predictor of the squared PC-1 timeseries.

Since $\mathbf{P}$ depends on multiple factors such as frequency (how often an event occurs), period (how long an event lasts) and wavelength of the disturbance, and trends in $\mathbf{P}$ alone do not necessarily reveal how a particular disturbance is changing over time. The filtered OLR data were also used to evaluate possible trends in anomaly characteristics in the given bands. The technique used here is similar to ones used in evaluating heatwave trends (e.g., Raghavendra et al. 2018b) where the frequency, intensity, and duration of heatwave events are calculated based on a threshold temperature. However, instead of using an arbitrary percentile threshold for filtered OLR representative of different equatorial waves, here we identify an event based on the spectrally filtered negative OLR anomaly present in the 38–year time series for each grid point between 15°N–15°S. This technique helps identify the frequency of occurrence, duration, and other measurements such as the mean OLR anomaly during the active phase of the disturbance (not shown since trends were mostly insignificant) for signals in the different wave filter bands.

The influence of El Niño–Southern Oscillation (ENSO) variability was accounted for by calculating the difference in the mean $\mathbf{P}$ for those time windows corresponding to a particular ENSO state based on the ERSSTv5 Niño 3.4 index (Huang et al. 2017) and the Niño 3.4 index data was obtained from NOAA's Climate Prediction Center (CPC; http://www.cpc.ncep.noaa.gov/data/indices/). The threshold for an El–Niño time windows was a mean Niño 3.4 index greater than 0.75, La–Niña if the mean Niño 3.4 index was less than −0.75, and ENSO neutral conditions if the mean Niño 3.4 index was between ±0.25.

Here we use three approaches to quantify the changes in the spectral $\mathbf{P}$ obtained from the OLR and T_b datasets. To quantify trends at the grid and regional mean levels, least squares regression was used to estimate the linear trend. The statistical significance (*p*–value) of the linear trend line was estimated by the two-tailed student's t-test. A Mann-Kendall (MK) test was applied in some case in conjunction with a linear

regression analysis to evaluate whether the trends are significant. Uncertainties in trends were captured by a Monte Carlo analysis. A two-sample t-test applied to the two pairs of populations to quantify if significant differences in **P** exist between the beginning and end of the datasets. In this study, *p*–value < 0.1 was adopted to be statistically significant.

4. Results

a) Changes in the mean spectrum

Using the techniques similar to WK99, Fig. 2 presents the mean normalized antisymmetric and symmetric parts of the **P** spectrum using both the OLR and T_b datasets. Both datasets are remarkably similar to each other and capture the peak in **P** corresponding to different types of wave activity observed in the tropical latitudes. These features are consistent with similar works published in the literature (e.g., Roundy 2018; WK99). While the spectra obtained from the OLR and T_b datasets may be similar, they are not identical given the nature of the datasets. For instance, around $k = 14$ the OLR dataset shows a local increase in **P** (Fig. 2a–b) and WK99 attributes this inconsistency to the polar orbiting satellite making approximately 14 swaths around the globe per day. By definition, the higher resolution geostationary satellites used to create the T_b dataset does not move relative to a fixed geographical location on the Earth, and instead uses multiple geostationary satellites to obtain a merged global picture (Knapp et al. 2011). In comparison to the OLR dataset, T_b dataset produces a smoother **P** spectrum with fewer spurious peaks (Fig. 2c–d).

In Fig. 3, we subtracted the mean of the first nine years from the mean of the most recent nine years of the **P** spectrum to identify any systematic shifts in the **P** spectrum. The results suggest a shift in **P** where the magnitude of **P** has increased in higher f signals (0.2–0.5 cycles per day; cpd, or 2 to 5-day period), and decreased in lower f signals (0.0–0.2 cpd, or >5-day period). In order to establish whether these trends are stable and significant in time, a latitude mean linear regression analysis was applied to the **P** spectrum (Fig. 4). Consistent with the results shown in Fig. 3–4 shows relatively weak yet significant increases in **P** between 0.2–0.5 cpd. While there are some patches of blue in Fig. 4 between 0.2–0.5 cpd indicative of a decreasing trend in **P**, these patches are characterized by an insignificant (p-value > 0.1) linear trend. Between 0–0.2 cpd, we observed a mixture of both positive and negative trends in **P** in Figs. 3–4. Overall, over 29% of the trends in Fig. 4 were statistically significant.

b) Trends in wave activity

Since the **P** spectrum captures many scales of motion observed in the tropical latitudes, by dividing the f and wavenumber **P** spectrum into different regions dominated by a particular phenomenon (WK99; Straub and Kiladis 2002; Roundy and Frank 2004, Kaladis et al. 2005, 2009), we may estimate how the characteristics of signals in bands of the wave number f domain associated with a given wave may have changed. In this study, we analyzed trends in five different kinds of disturbances observed in the tropical latitudes i.e., MJO, ER waves, MRG waves, Kelvin waves, and TD-type disturbances from both the OLR and T_b datasets (Fig. 5). The trends in **P** for a given wave type closely follow the predominant trend for a given f since there is little variability across k for $\sim$0.2 cpd or higher (Fig. 4). In general, lower f (0–0.2 cpd) is losing **P**, and higher f (0.2–0.5 cpd) is gaining **P**. The MJO and ER wave suggest decreasing trends in **P**, but only the symmetric part of the **P** spectrum for the T_b dataset showed a statistically significant decrease. The other three wave types that are dominated by relatively higher f and are characterized by localized regions of significant **P** increases below 0.2 cpd mostly show statistically significant increasing trends in **P**.

As the spatial structure and trends obtained from the OLR and T_b datasets compare well with each other (Raghavendra et al. 2018a), we were not surprised to observe similar trends from the two datasets (Figs. 2–5). Figure 6 provides confidence thresholds for the slope of the curves in Fig. 5. Since the amplitude of the interannual variability is relatively high when compared to the net long-term change in **P** (i.e., low signal to noise ratio), we observe a relatively large range of values making up the 5–95% confidence interval. Except for the symmetric part of the MJO and ER wave for the OLR dataset that coincidently have the highest p–value (least significant) linear trend in Fig. 5, the confidence intervals concur with the net change in sign for the observed trends in the **P** spectrum (Fig. 5–6). As expected from the results illustrated in Figs. 3–4, the MJO and ER wave have lost **P**, and Kelvin waves, MRG, and TD–type waves have gained **P**. The linear trend analysis (Fig. 5) and confidence range (Fig. 6) also support the above conclusion.

c) Trends in variance and trends in the leading modes of variability

We have thus far shown time trends in spectral power (Figs. 3–6). Furthermore, the spatial structure corresponding to the trends in OLR variance (Fig. 7) appears to be concentrated near regions characterized by a peak in annual mean variance presented in Kiladis et al. (2009). However, there is a possibility that trends in background noise may be strongly projecting onto the trends in spectral power (Figs. 3–6), and thus making it unclear whether wave signals are changing in a similar manner. To address this concern, an EOF analysis was conducted to evaluate if patterns in the data conforming to the structures of convectively coupled waves change amplitude with time, via assessment of trends in variance of the PC-1 timeseries.

The spatial structure of the leading EOF (EOF-1) explains the maximum variance (Fig. 8) and the EOF-1 spatial pattern for MRG waves (Fig. 8d) closely resembles the MRG wave pattern in Kiladis et al. (2009). Since the amplitude of a leading EOF mode and preferred structure pattern can change over time,

we compared the same analysis based on EOFs computed based on the first (1979–1993) and last (2002–2016) 15-year periods from the OLR dataset and found negligible differences in the spatial structure of the leading EOFs, and trends in variance corresponding to PC1 were not statistically distinguishable from the trends in PCs based on EOF patterns computed from the entire dataset (Figs. 8–9). The trends in variance corresponding to PC1 for five different wave types are shown in Fig. 9. In this figure, we observe large interannual variability, a significant decrease in variance for the MJO band, and a significant increase in variance for KWs, MRG waves, and TD-type disturbances. An insignificant increasing trend is observed for ERWs. The trends from Fig. 9 compare favorably with Figs. 5–6, and Fig. 7, and we find mutually supporting evidence for four wave types (except ERW where the trend lines are not statistically significant). In summary, the analysis presented in Figs. 8–9 shows that signals that project onto the leading EOF mode trend similarly to variance in the filter bands themselves and proving that the waves themselves are part of the trend. So, regardless of whether background noise is trending, the wave signals are trending in the same direction as variance in the bands.

d) Spatial trends in wave activity

This sub-section is motivated because we now understand changes in the **P** spectrum for over 35 years, and the trends in **P** associated with five tropical wave types, but we lack physical insight on how individual wave characteristics (i.e., trends in the number of events, and the duration of an events) corresponding to the five different spectral band many have changed. Furthermore, understanding spatial trends in wave activity, and the mean duration of the active period corresponding to a given wave may help us better understand mechanisms regulating tropical convection and precipitation. By identifying the convective phase for different wave types and calculating the occurrence and mean duration of an event (Fig. 10), we find those wave bands characterized by an increase in power at high f (e.g., KWs, MRG, and TD-type) show a significant upward trend in the mean number of events and accompanied by a decrease the mean duration of an event. There are fewer grid points showing significant trends for the MJO and ERW spectral bands, but the spatial distribution of trends in event occurrence and duration (Fig. 10 a–b and c–d) suggests a compensating effect between frequency and duration resulting in a tendency towards a homogeneous spatial field. To further elaborate, considering the MJO band, for instance, there is good agreement between observed trends (Fig 10a) and modeling efforts using GCMs (e.g., Jones and Carvalho 2006; Arnold et al. 2015; Song and Seo 2016; Adams et al. 2017) in the increased occurrence of MJO events attributed to global warming. While it is generally argued that MJO intensity will likely increase in a warmer climate, both observations and modeling studies discuss considerable uncertainties with regard to intensity and duration changes in the MJO. Furthermore, there are non-negligible biases in GCM realizations of the mean background state of the tropical atmosphere. Some of these issues include a cold bias for SSTs in atmosphere-ocean coupled runs, the double ITCZ problem (e.g., Lin 2007), and overestimated tropical OLR variability (e.g., Arnold et al. 2015). Therefore, while Fig. 5a–b suggests a negative trend in **P** corresponding to the MJO, this does not imply a weakening MJO, or less frequently occurring MJO. However, the reduction in **P** corresponding to the MJO does imply a reduced variance in the MJO (Fig. 7a), therefore either a reduction of amplitude, and/or a reduction of the longevity of active periods must be occurring (Fig. 10a–b). Fig. 3–4 suggests a shift in the MJO band towards higher frequencies, but additional analysis beyond the scope of this paper on how changes in the combination of the amplitude and/or longevity of active periods of equatorial waves both on a regional and global scale may explain the observed trends in **P**.

e) ENSO's impact on the power spectrum

Variability in ENSO is known to strongly influence tropical convection and a key player in climate variability (e.g., WK99; Neale et al. 2008). Not surprisingly, since tropical wave activity and convection are strongly coupled, variability in ENSO could strongly influence tropical waves and the trends in wave activity we observed in Figs. 3–6. In order to better understand the impact of ENSO on the f and k **P** spectrum, we constructed difference plots (Fig. 11) between the mean spectrum for a given ENSO state and the total **P** spectrum (Fig. 2). Changes in **P** associated with El–Niño include enhanced KW, an increase in higher f, a decrease in lower f for eastward propagating wave activity, and weaker TD-type disturbance activity. La-Niña shows the opposite effects. No coherent patterns in wave activity were observed for ENSO neutral state. While the six individual panels are significantly different from each other both in terms of structure and power, we are not convinced that the structure of the **P** spectrum corresponding to different phases of ENSO could possibly produce the trends in **P** shown in Figs. 3–6.

5. Conclusions and Remarks

In this study, the f and k **P** spectrum for the tropical latitudes (i.e., 15°N–15°S) was constructed using the method outlined by WK99 for OLR data obtained from polar orbiting satellites (Liebmann and Smith 1996), and T_b data obtained from geostationary satellites (Knapp et al., 2011). Both datasets produced **P** spectra that are similar to one another (Fig. 2). Since the fundamental goal of the paper was to identify changes in the f and k **P** spectrum, we subtracted the **P** spectrum of the first nine years from that of the last nine years to investigate possible changes in the **P** spectrum (Fig. 3). This exercise revealed a significant decrease in **P** from ~0–0.2 cpd, and an increase in **P** from ~0.2–0.5 cpd. The significance of the trend was

also established via a linear regression (Fig. 4). Since different parts of the f and k **P** spectrum are associated with different waves observed in the tropical latitudes (e.g., Kiladis et al. 2009), we averaged the **P** corresponding to regions of the spectrum known to be occupied by signals from particular wave types and examined the trends.

Given the low signal to noise ratio observed with the **P** trends in Fig. 5 and to quantify uncertainties in the results, a Monte Carlo analysis was carried out (Fig. 6). We found the bands of the MJO and the ER wave were characterized by a decreasing trend in **P**, and the bands of MRG waves, Kelvin waves, and TD-type disturbances were characterized by increasing trends in **P** (Fig. 5–6). From Figs. 3–5, we infer an increase in variability at higher frequencies attributed to an increase in **P** and vice-versa. To further evaluate the validity of the change in **P** reported thus far and to ensure the changes in spectral power were linked to the waves and not the background "noise", we evaluated trends in band filtered daily OLR anomaly data from 1979–2016 for variance (Fig. 7), the structure of the leading EOF pattern (Fig. 8), and trends in the variance corresponding to PC-1. The PC analysis shows that signals that project onto the leading EOF mode trend similarly to variance in the filter bands themselves and demonstrate that the waves themselves are part of the trend. Therefore, concurrence between the time trends in the variance corresponding to the first principle component (PC1; Fig. 9) and spectral power (Figs. 5–6) should bolster our confidence in the results and help us draw to the conclusion that the trends in spectral power for each wave type is a consequence of changes in the wave characteristics, and not just background noise.

A possible relationship between changes in **P** and changes in the frequency of occurrence and mean duration of wave events was also presented (Fig. 10). Results suggests the it may be possible to attribute that the increase in power at high f (e.g., KWs, MRG, and TD-type) to a significant increase in the occurrence of high frequency disturbances, accompanied by a decrease the mean duration of an event. The results for a decrease in power at low f (e.g., MJO and ERW) is difficult to explain given non-homogeneous trends in the mean duration of the events. Finally, we demonstrate the influence of ENSO on the **P** spectrum (Fig. 11) and argue that the trends in **P** documented in Figs. 3–5 are difficult to explain from the standpoint of variability in ENSO.

Our future research endeavors include diagnosing changes in the characteristics of tropical waves (e.g., f, amplitude, and persistence), and identifying mechanisms resulting in the observed change in the **P** spectrum. The subset of our community that specialized in climate variability and change has published a considerable spectrum of works to better understand Earth's atmosphere and ocean dynamics across different spatio-temporal scales. Therefore, there are many possible future research avenues to understand mechanisms linked to changes in tropical waves and the associated f-wavenumber **P** spectrum presented in this paper (Fig. 3–6). Some of these research avenues and possible mechanisms that may explain changes and trends in tropical wave activity include:

- The impacts of a narrowing ITCZ, changes in the breakdown of the ITCZ, and expanding Hadley cell (e.g., Byrne and Schneider 2016; Raghavendra and Guinn 2016).
- Changes in the profile of ocean heat transport and associated changes in the Hadley cell (Rencurrel and Rose 2018).
- An observed enhancement in the tropical Walker cell circulation associated with an increased temperature contrast between regions within the tropical latitudes (e.g., Kosaka and Xie 2013; Meng et al. 2012; Hua et al. 2016; Ma and Zhou 2016; Zhang and Karnauskas 2017).
- Localized and non-localized convection/heating within the tropical latitudes (e.g., Neale and Hoskins 2001; Raghavendra and Guinn 2016; Raghavendra et al. 2018a) and associated Gill–Matsuno and tropical waves response to steady tropical heating (e.g., Cook and Vizy 2016).
- Extratropical influences, especially given recent studies highlighting arctic amplification and changes in the midlatitude Rossby wave train (e.g., Barnes and Polvani 2015) can alter the eddy momentum fluxes between the tropical and extratropical latitudes and consequently impact the monsoon and the large scale tropical circulation (e.g., Schneider and Bordoni 2008; Bordoni and Schneider 2010).
- Teleconnections such as Pacific decadal oscillation and North Atlantic oscillation may also prove to be useful endeavors to better understand convectively coupled equatorial waves.

Finally, current climate models are relatively poor in capturing observed tropical precipitation characteristics (e.g., Dai 2006) but may capture the dynamics of free and convectively coupled tropical waves to varying degrees of accuracy (e.g., Hung et al. 2013). Understanding the linkage between tropical waves and precipitation, and using projected changes in tropical wave activity to estimate precipitation change maybe a worthwhile exercise as well. A hierarchical modeling approach (e.g., Isca; Vallis et al. 2018) ranging from idealized to fully coupled GCMs may prove particularly useful in isolating mechanisms linked to the observed and possible future changes in the f-wavenumber **P** spectrum. From a climate change and societal impact perspective, analyzing precipitation changes linked to the observed and projected changes in the dynamics of tropical wave activity over may offer insights on the water budget and availability over tropical latitudes.

Acknowledgements.
AR and LZ were supported by the National Science Foundation (NSF) AGS-1535426. PR would like to

acknowledge the support received from NSF-AGS1358214 and AGS-1128779. We would like to thank Dr. Juliana Dias for insightful discussions that helped improve our work. Gratitude is also extended to Ms. Kaitlyn N. Krzyzaniak for suggestions that improved the quality of this paper. We sincerely thank five anonymous reviewers, and Dr. Tim Li (Editor) for their constructive criticism, and suggestions which improved the clarity and quality of this work submitted to the *Journal of Climate*.

References

Adames, A. F., Kim, D., Sobel, A. H., Del Genio, A., & Wu, J. (2017). Characterization of moist processes associated with changes in the propagation of the MJO with increasing CO2. *J. Adv. Model. Earth Syst.,* **9,** 2946–2967.

Arnold, N., M. Branson, Z. Kuang, D. A. Randall, and E. Tziperman, 2015: MJO intensification with warming in the Super-Parameterized CESM. *J. Climate,* **28,** 2706–2724.

Barnes, E. A., and L. M. Polvani, 2015: CMIP5 projections of Arctic amplification, of the North American/North Atlantic circulation, and of their relationship. J. Climate, 28, 5254–5271.

Barton, I. J., 1995: Satellite-derived sea surface temperatures: Current status. *J. Geophys. Res.,* **100,** 8777–8790.

Bordoni, S., and T. Schneider, 2010: Regime transitions of steady and time-dependent Hadley circulations: Comparison of axisymmetric and eddy-permitting simulations. *J. Atmos. Sci.,* **67,** 1643–1654.

Byrne, M. P. and Schneider, T., 2016. Narrowing of the ITCZ in a warming climate: physical mechanisms. *Geophys. Res. Lett.,* **43,** 11,350–11,357.

Cai, W., and Coauthors, 2015: Increased frequency of extreme La Niña events under greenhouse warming. *Nature Climate Change,* **5,** 132–137.

Chen, G. H., and R. H. Huang, 2009: Interannual variations in mixed Rossby–gravity waves and their impacts on tropical cyclogenesis over the western North Pacific. *J. Climate,* **22,** 535–549.

Cook, K. H., and Vizy, E. K., 2016: The Congo Basin Walker circulation: dynamics and connections to precipitation. *Climate Dyn.,* **47,** 697–717.

Dai, A., 2006: Precipitation characteristics in eighteen coupled climate models. *J. Climate,* **19,** 4605–4630.

Francis, J. A., and S. J. Vavrus, 2012: Evidence linking Arctic amplification to extreme weather in mid-latitudes. *Geophys. Res. Lett.,* **39,** L06801.

Frigo, M., and S. G. Johnson, 2005: The Design and Implementation of FFTW3. *Proceedings of the IEEE,* **93,** 216–231.

Frigo, M., and S. G. Johnson, 1998: FFTW: An Adaptive Software Architecture for the FFT. *Proc. Int. Con. Acoust. Speech, Signal Process.,* **3,** 1381–1384.

Garcia, D., 2010: Robust smoothing of gridded data in one and higher dimensions with missing values. *Comput. Statist. Data Anal.,* **54,** 1167–1178.

Holton, J. R., and G. J. Hakim, 2013: An Introduction to Dynamic Meteorology. Elsevier Academic Press, 532 pp.

Hua, W., L. Zhou, H. Chen, S. Nicholson, A. Raghavendra, and Y. Jiang, 2016: Possible Causes of the Central Equatorial African Long-term Drought. Environ. Res. Lett., **11,** 124002.

Hua, W., L. Zhou, H. Chen, S. E. Nicholson, Y. Jiang, A. Raghavendra, 2018: Understanding the Central Equatorial African long-term drought using AMIP-type simulations. *Climate Dyn.,* **50,** 1115–1128.

Huang, B., and Coauthors, 2017: Extended Reconstructed Sea Surface Temperature, Version 5 (ERSSTv5): Upgrades, Validations, and Intercomparisons. *J. Climate,* **30,** 8179–8205.

Huang, P., and R. H. Huang, 2011: Climatology and Interannual Variability of Convectively Coupled Equatorial Waves Activity. *J. Climate,* **24,** 4451–4465.

Hung, M.-P., J.-L. Lin, W. Wang, D. Kim, T. Shinoda, and S. J. Weaver, 2013: MJO and convectively coupled equatorial waves simulated by CMIP5 climate models. *J. Climate,* **26,** 6185–6214.

Jones, C., and L. M. V. Carvalho, 2006: Changes in the Activity of the Madden–Julian Oscillation during 1958–2004. *J. Climate,* **19,** 6353–6370.

Jiang, Y., L. Zhou, C. J. Tucker, A. Raghavendra, W. Hua, Y. Liu, J. Joiner, 2018: Widespread increase of boreal summer dry season length observed over the Congo Rainforest in the last three decades. *Nature Climate Change* (in review)

Joyce, R., Janowiak, J., and Huffman, G., 2001: Latitudinally and Seasonally Dependent Zenith-Angle Corrections for Geostationary Satellite IR Brightness Temperatures. *J. Appl. Meteor.,* **40,** 689–703.

Kiladis, G. N., K. H. Straub, P. T. Haertel, 2005: Zonal and vertical structure of the Madden–Julian oscillation. *J. Atmos. Sci.,* **62,** 2790–2809.

Kiladis, G. N., M. C. Wheeler, P. T. Haertel, K. H. Straub, P.E. Roundy, 2009: Convectively coupled equatorial waves. *Rev. Geophys.,* **47,** RG2003.

Knapp, K. R., 2008: Scientific data stewardship of International Satellite Cloud Climatology Project B1 global geostationary observations. *J. Appl. Remote Sensing,* **2,** 023548,

Knapp, K. R., and Coauthors, 2011: Globally gridded satellite (GridSat) observations for climate studies. *Bull. Amer. Meteor. Soc.,* **92,** 893–907.

Kosaka, Y., and Xie, S. P., 2013: Recent global-warming hiatus tied to equatorial Pacific surface cooling. *Nature,* **501,** 403–407.

Lewis, S. L., 2006: Tropical forests and the changing earth system. *Phil. Trans. R. Soc. Lond. B,* **361,** 195–210.

Li, J., K. Fan, and L. Zhou, 2017: Satellite observations of El Nino impacts on Eurasian spring vegetation greenness during the period 1982-2015. *Remote Sens.,* **9,** 628.

Liebmann, B and C. A. Smith, 1996: Description of a Complete (Intropolated) Outgoing Lonfwave Radiation Dataset. *Bull. Amer. Meteor. Soc.*, **77**, 1275–1277.

Lin, J.-L., and Coauthors, 2006: Tropical Intraseasonal Variability in 14 IPCC AR4 Climate Models. Part I: Convective Signals. *J. Climate,* **19,** 2665–2690.

Lin, J.-L., 2007: The double-ITCZ problem in IPCC AR4 coupled GCMs: Ocean–atmosphere feedback analysis. *J. Climate,* **20,** 4497–4525.

Ma, S., and Zhou, T., 2016: Robust strengthening and westward shift of the tropical Pacific Walker circulation during 1979–2012: A comparison of 7 sets of reanalysis data and 26 CMIP5 models. *J. Climate,* **29,** 3097–3118.

Madden, R. and P. Julian, 1971: Detection of a 40-50 day oscillation in the zonal wind in the tropical Pacific, *J. Atmos. Sci.*, **28**, 702–708.

Madden R. and P. Julian, 1972: Description of global-scale circulation cells in the tropics with a 40-50 day period. *J. Atmos. Sci.*, **29**, 1109–1123.

Meng, Q., M. Latif, W. Park, N. S. Keenlyside, V. A. Semenov, and T. Martin, 2012: Twentieth century Walker circulation change: Data analysis and model experiments. *Climate Dyn.,* **38,** 1757–1773.

National Research Council (NRC), 2004: Climate Data Records from Environmental Satellites. National Academies Press, Washington, DC. 150 pp.

Neale, R. B. and Hoskins, B. J., 2000: A standard test for AGCMs including their physical parametrizations. II: results for the Met Office Model. *Atmos. Sci. Lett.,* **1,** 108–114.

Neale, R. B., J. H. Richter, and M. Jochum, 2008: The impact of convection on ENSO: From a delayed oscillator to a series of events. *J. Climate,* **21,** 5904–5924.

Raghavendra, A., L. Zhou, Y. Jiang, and W. Hua, 2018a: Increasing Extent and Intensity of Thunderstorms Observed Over the Congo from 1982–2016. *Atmos. Res.,* **213,** 17–26.

Raghavendra, A., A. Dai, S. M. Milrad, and S. R. Cloutier-Bisbee, 2018b: Floridian Heatwaves and Extreme Precipitation: Future Climate Projections. *Climate Dyn,* in press, doi: 10.1007/s00382-018-4148-9

Raghavendra, A., and T. A. Guinn, 2016: Breakdown of ITCZ-like PV Patterns. *Beyond: Undergrad. Res. J.,* **1,** 1–11.

Rencurrel, M. C., and B. E. J. Rose, 2018: Exploring the climatic response to wide variations in ocean heat transport on an aquaplanet. *J. Climate,* **31,** 6299–6318.

Rose, B. E. J., K. C. Armour, D. S. Battisti, N. Feldl, and D. D. B. Koll, 2014: The dependence of transient climate sensitivity and radiative feedbacks on the spatial pattern of ocean heat uptake. *Geophys. Res. Lett.,* **41,** 1071–1078.

Roundy P. E., and Frank W. M., 2004: A climatology of waves in the equatorial region. *J. Atmos. Sci.,* **61,** 2105–2132.

Roundy, P. E., 2017: Diagnosis of seasonally varying regression slope coefficients and application to the MJO. *Q.J.R. Meteorol. Soc.,* **143,** 1946–1952.

Roundy, P. E., 2018: A wave-number frequency wavelet analysis of convectively coupled equatorial waves and the MJO over the Indian Ocean. *Q.J.R. Meteor*

Schiffer, R.A., and Rossow, W.B., 1983. The International Satellite Cloud Climatology Project (ISCCP): The First Project of the World Climate Research Programme. *Bull. Amer. Meteor. Soc.,* **64,** 779–784.

Schiraldi, N. J., and P. E. Roundy, 2017: Seasonal-to-Subseasonal Model Forecast Performance during Agricultural Drought Transition Periods in the U.S. Corn Belt. *Mon. Wea. Rev.,* **145,** 3687–3708.

Schmetz, J., Tjemkes, S. A., Gube, M., and van de Berg, L., 1997. Monitoring deep convection and convective overshooting with METEOSAT. *Adv. Space Res.,* **19,** 433–441.

Schneider, T., and S. Bordoni, 2008: Eddy-mediated regime transitions in the seasonal cycle of a Hadley circulation and implications for monsoon dynamics. *J. Atmos Sci.,* **65,** 915–934.

Straub, K. H., G. N. Kiladis, 2002: Observations of a Convectively Coupled Kelvin Wave in the Eastern Pacific ITCZ. *J. Atmos. Sci.,* **59,** 30–53.

Song, E.-J., and K.-H. Seo, 2016: Pastand present-day Madden-Julian Oscillation in CNRM-CM5. *Geophys. Res. Lett.,* **43,** 4042–4048.

Trenberth, K. E., and D. P. Stepaniak, 2004: The flow of energy through the earth's climate system *Q.J.R. Meteorol. Soc.,* **130,** 2677–2701.

Vallis, G. K., and Coauthors, 2018: Isca, v1.0: a framework for the global modelling of the atmospheres of Earth and other planets at varying levels of complexity, *Geosci. Model Dev.,* **11,** 843–859.

Wang, G., D. Garcia, Y. Liu, R. de Jeu, and A. J. Dolman, 2012: A three- dimensional gap filling method for large geophysical datasets: Application to global satellite soil moisture observations. *Environ. Modell. Softw.,* **30,** 139–142.

Wang, L., and T. Li, 2017: Roles of convective heating and boundary-layer moisture asymmetry in slowing down the convectively coupled Kelvin waves. *Climate Dyn.,* **48,** 2453–2469.

Wang, L., and L. Chen, 2016: Interannual variation of convectively-coupled equatorial waves and their association with environmental factors. *Dyn. Atmos. Oceans,* **76,** 116–126.

Wei, N., L. Zhou, and Y. Dai, Y., 2017: Observational evidence for desert amplification using multiple satellite datasets. *Scientific Reports,* **7,** 2043.

Wheeler, M., and G.N. Kiladis, 1999: Convectively Coupled Equatorial Waves: Analysis of Clouds and Temperature in the Wavenumber-Frequency Domain. *J. Atmos. Sci.,* **56,** 374–399

Zhang, L., and Karnauskas, K. B., 2017: The role of tropical interbasin SST gradients in forcing Walker circulation trends. *J. Climate,* **30,** 499–508.

Zhou, L., and Coauthors, 2014. Widespread decline of Congo rainforest greenness in the past decade. *Nature,* **509,** 86–90.

Figures

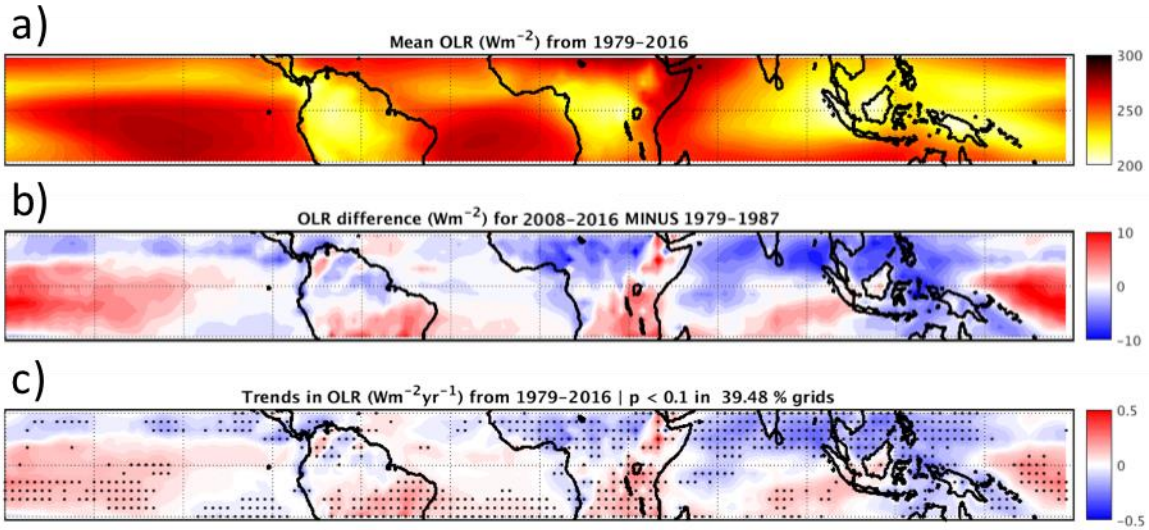

Figure 1: Global tropical convection (15°N–15°S) from 1979–2016 using NOAA's daily Interpolated OLR dataset (Liebmann and Smith 1996). a) Daily mean OLR, b) the difference in OLR between 1979–1987 and 2008–2016, and c) linear trends in OLR obtained after removing the seasonal cycle from the OLR dataset. The black dots indicate trends that are statistically significant (p-value<0.1).

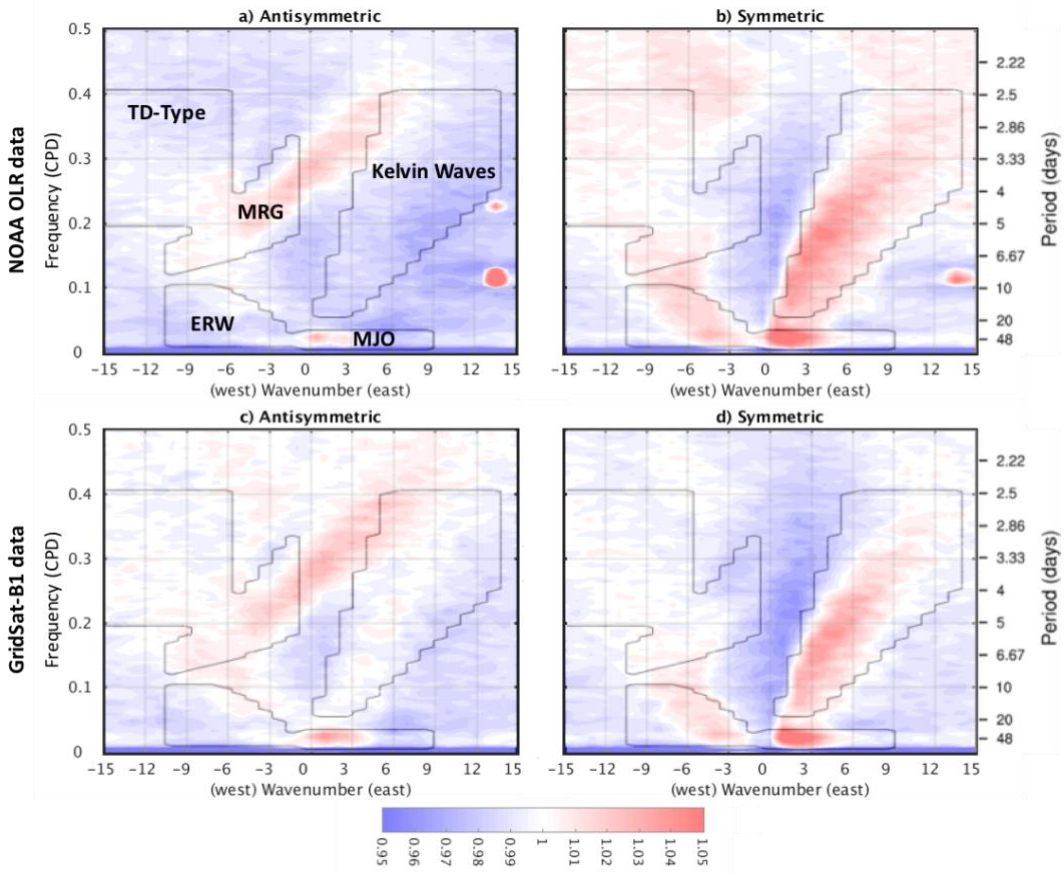

Figure 2: The frequency-wavenumber power spectrum diagram normalized by the smoothened background spectrum similar to the technique developed by WK99. The individual panels represent the antisymmetric power spectrum using the a) OLR and c) T_b datasets, and symmetric power spectrum using the b) OLR and d) T_b datasets.

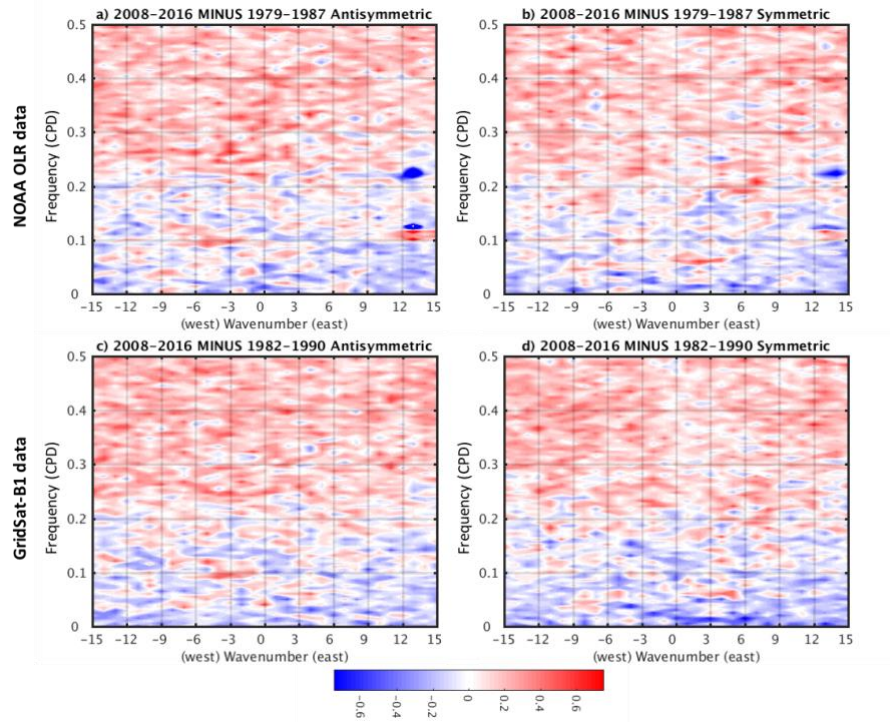

Figure 3: Observed shift in the $\log_e$ spectral power calculated by taking the difference between the mean normalized power for 2008–2016 and 1979–1987 (for OLR dataset)/1982–1990 (for T_b dataset). The individual panels represent the antisymmetric power spectrum using the a) OLR and c) T_b datasets, and symmetric power spectrum using the b) OLR and d) T_b datasets. A *two-sample t-test* applied to the two pairs of populations proved that the power for 2008–2016 is significantly different from the power for 1979–1987 at the 1% significance level.

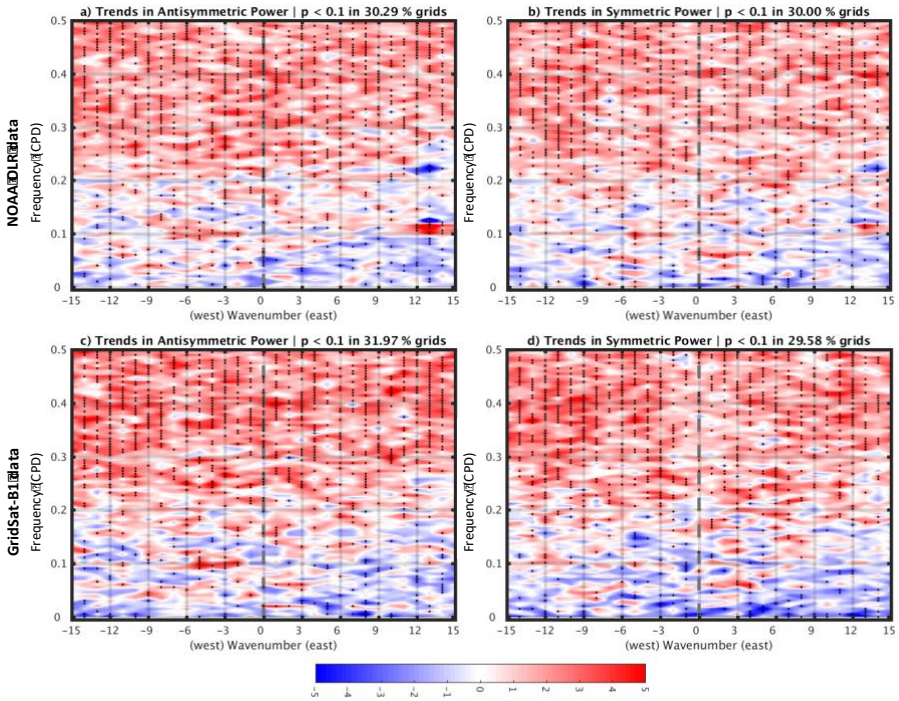

Figure 4: Linear trends in the $\log_e$ spectral power ($\times 10^{-3}$) from 1979–2016 for the OLR dataset and 1982–2016 for the T_b dataset. The individual panels represent the antisymmetric power spectrum using the a) OLR and c) T_b datasets, and symmetric power spectrum using the b) OLR and d) T_b datasets. The black dots indicate trends that are statistically significant (p-value<0.1).

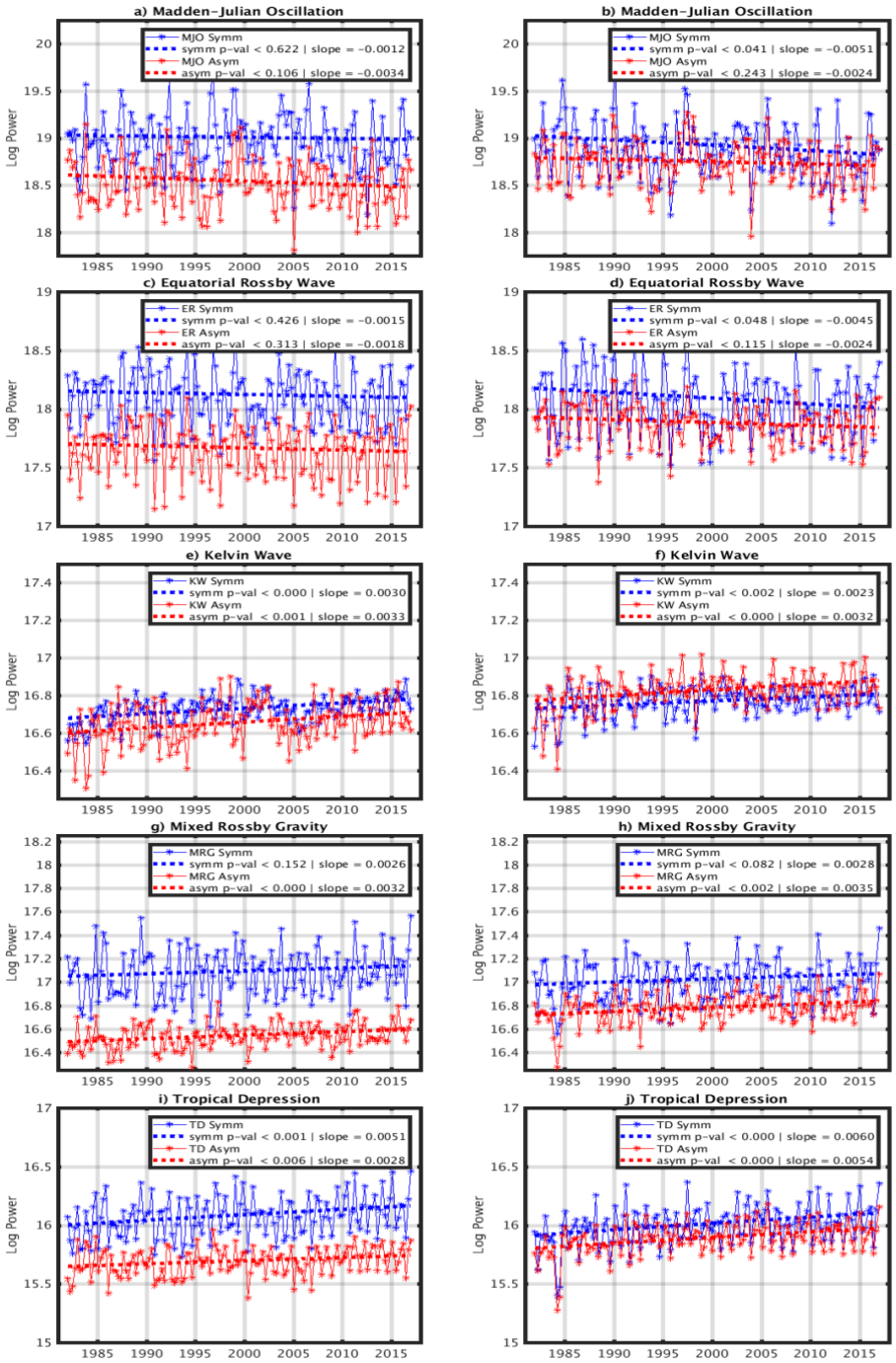

Figure 5: Interannual variations in the regional (see Fig. 2 for domain) mean $\log_e$ power spectrum (red for antisymmetric part, and blue for symmetric part) corresponding to different wave types in the WK99 frequency-power spectrum diagram using the (a–e) OLR, and T_b datasets. The slope, and the p-value (*p-val*) of the linear trend lines are shown in the box for each panel.

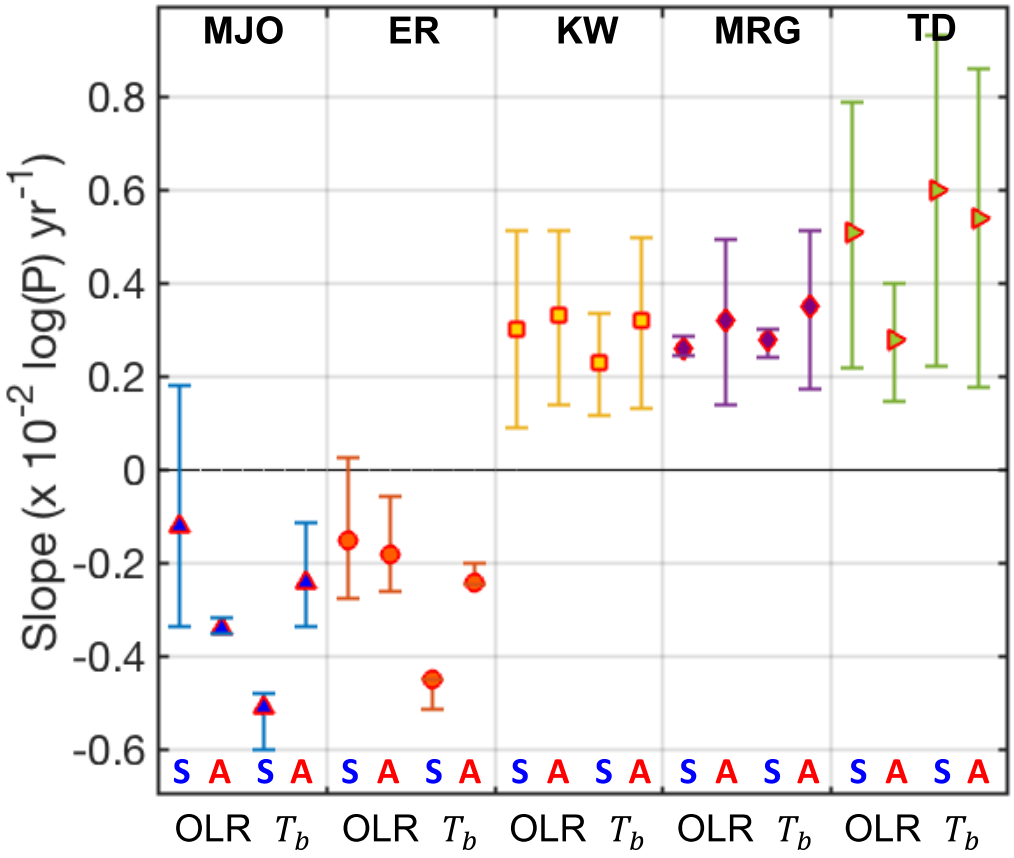

Figure 6: A Monte Carlo analysis carried out by randomly rearranging the data points for each interannual variability curve 1,000 times in Fig. 5 without repetition in order to quantify uncertainties in the slope (*units*: $\times 10^{-2} \log_e(\mathbf{P})\, year^{-1}$) of the linear trend line shown in Fig. 5. The upper (95th percentile) and lower (5th percentile) limits of the uncertainty is represented by the top and bottom whiskers respectively, and the slope values for the symmetric (S) and antisymmetric (A) components from Fig. 5 are represented using five symbols for each type of disturbance using both the OLR and T_b datasets.

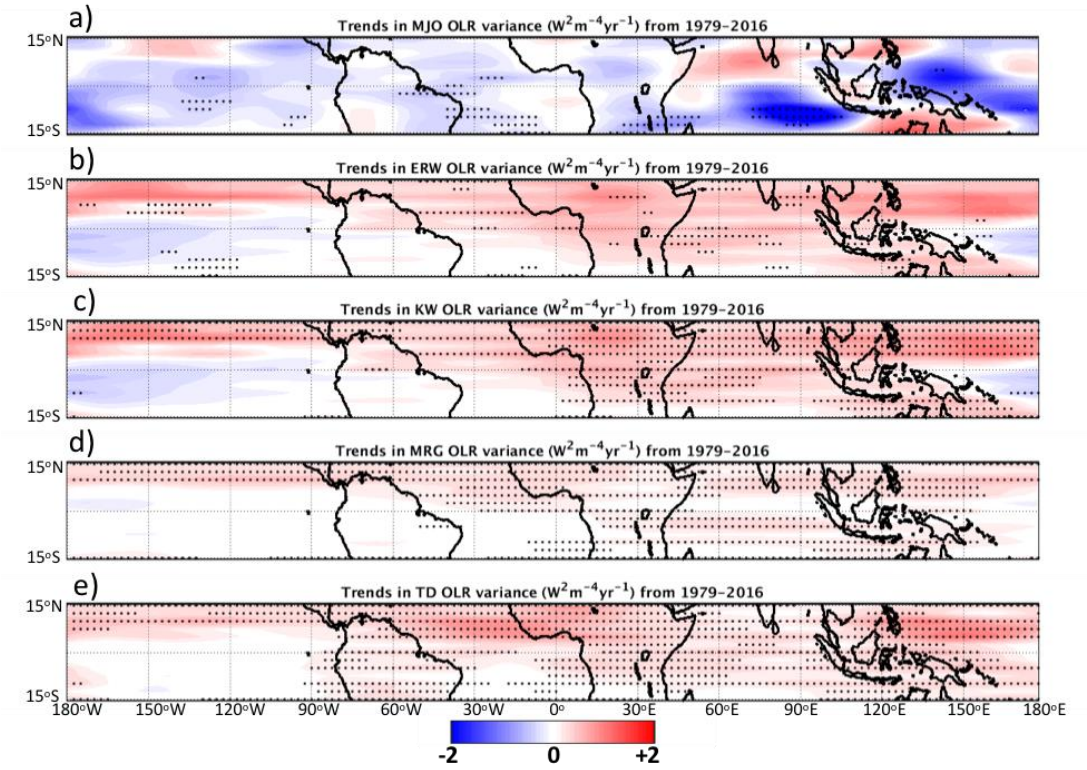

Figure 7: Trends in OLR variance calculated by squaring the spectrally filtered OLR anomaly for a) the MJO, b) ERW, c) KWs, d) MRG, and e) TD from 1979–2016. The black dots indicate trends that are statistically significant (p-value<0.1).

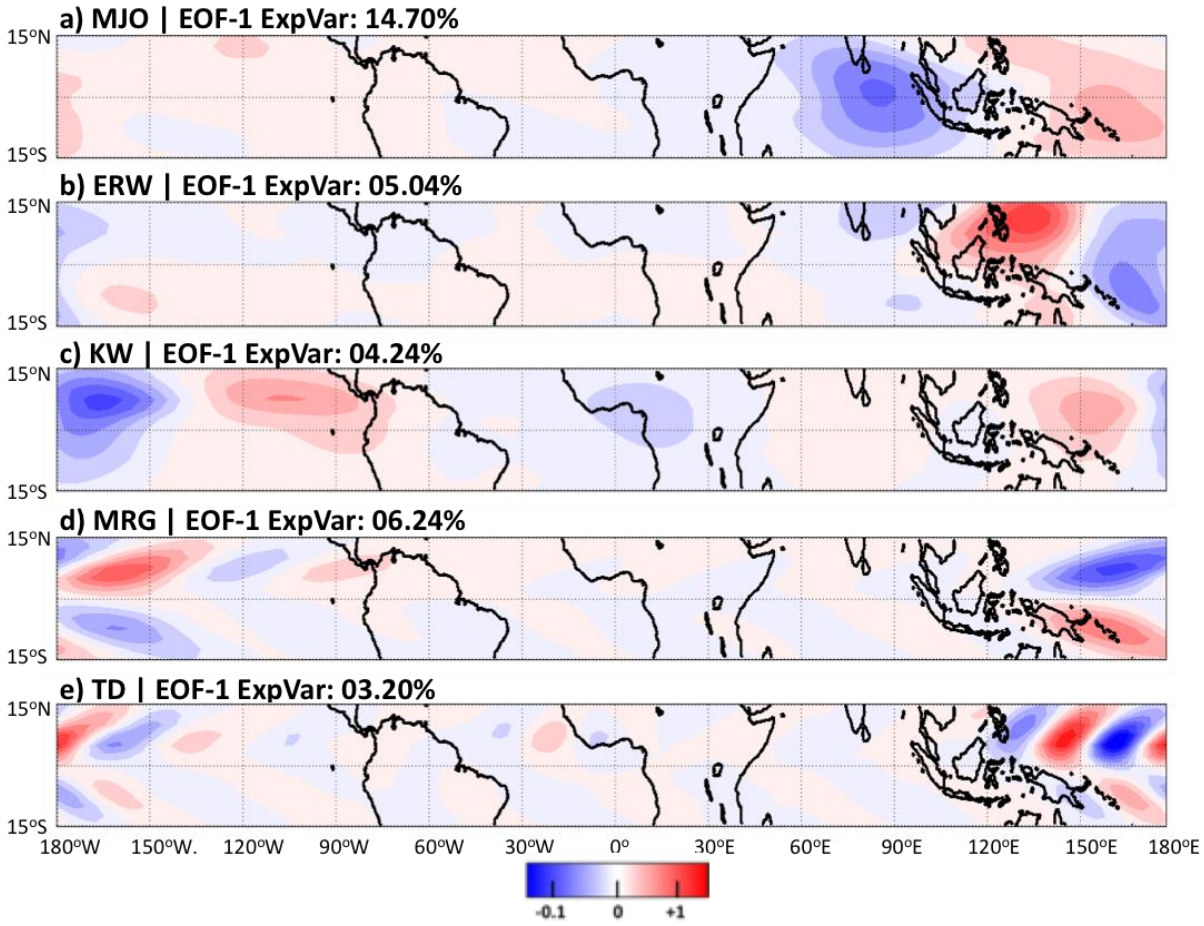

Figure 8: The spatial structure corresponding to the leading EOF for a) the MJO, b) ERW, c) KWs, d) MRG, and e) TD obtained by first filtering the daily OLR anomaly data from 1979–2016 for the five different wave bands, and then applying an EOF analysis. The percentage variance explained by the leading EOF are show in each panel.

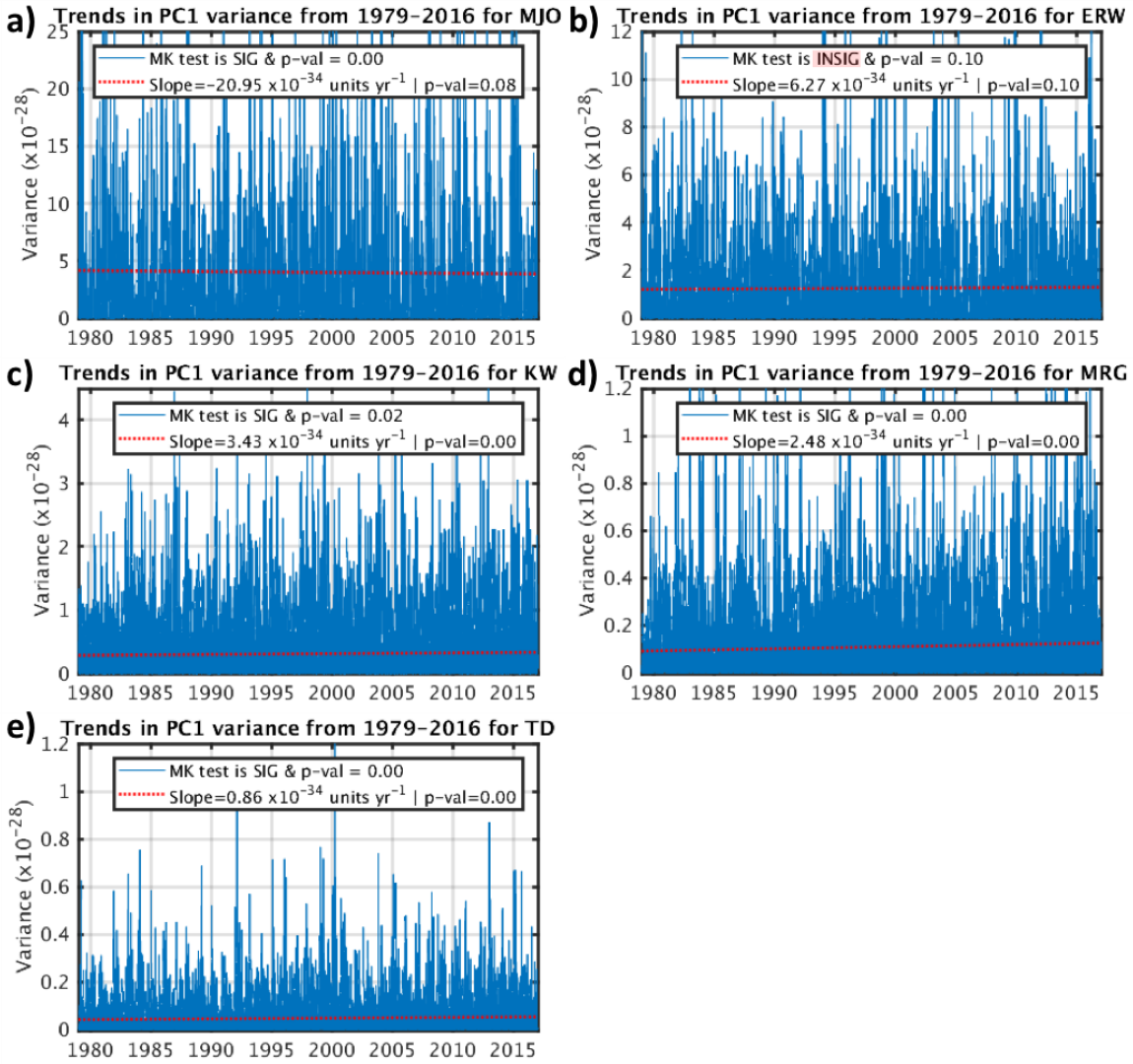

Figure 9: Interannual variability of the variance corresponding to first PC of the band filtered daily OLR anomaly data from 1979–2016 (blue line) for a) the MJO, b) ERW, c) KWs, d) MRG, and e) TD. The slope, and the p-value (*p-val*) of the linear trend lines (red line), and the result and p-value from the Mann-Kendall trend test are shown in the box embedded in each panel. The spatial structure corresponding to the leading EOF for each wave is shown in Fig. 8.

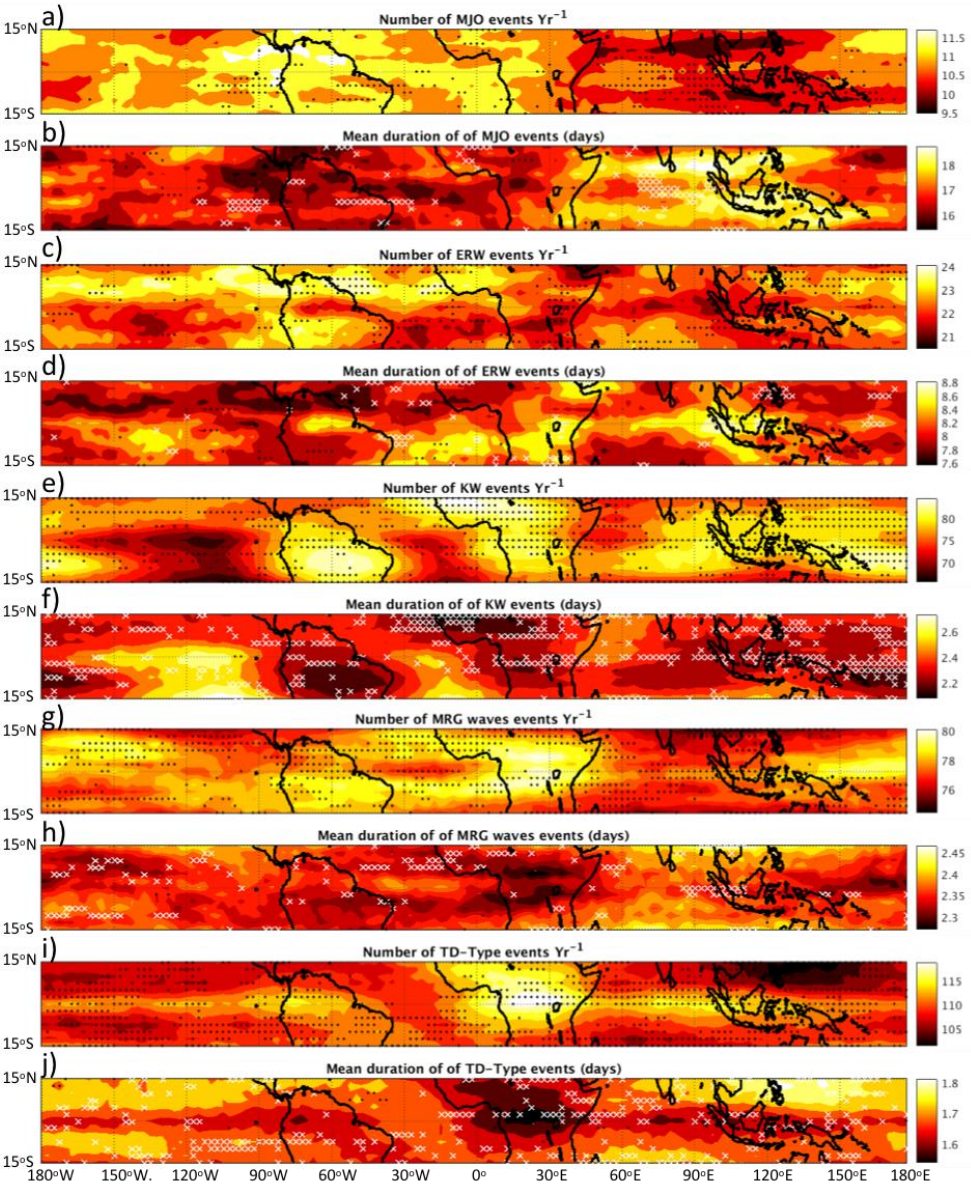

Figure 10: The mean number, and duration of events corresponding to (a–b) the MJO, (c–d) ERW, (e–f) KWs, (g–h) MRG, and (i–j) TD from 1979–2016 using daily OLR anomalies. The mean frequency and duration of events was calculated by applying a spectral filter for different wave types, and then using the negative OLR anomaly time series at each grid point to generate the necessary statistics. A linear regression and t-test was applied to determine regions showing significant ($p<0.1$) increasing (black dot) and decreasing (white cross) trends.

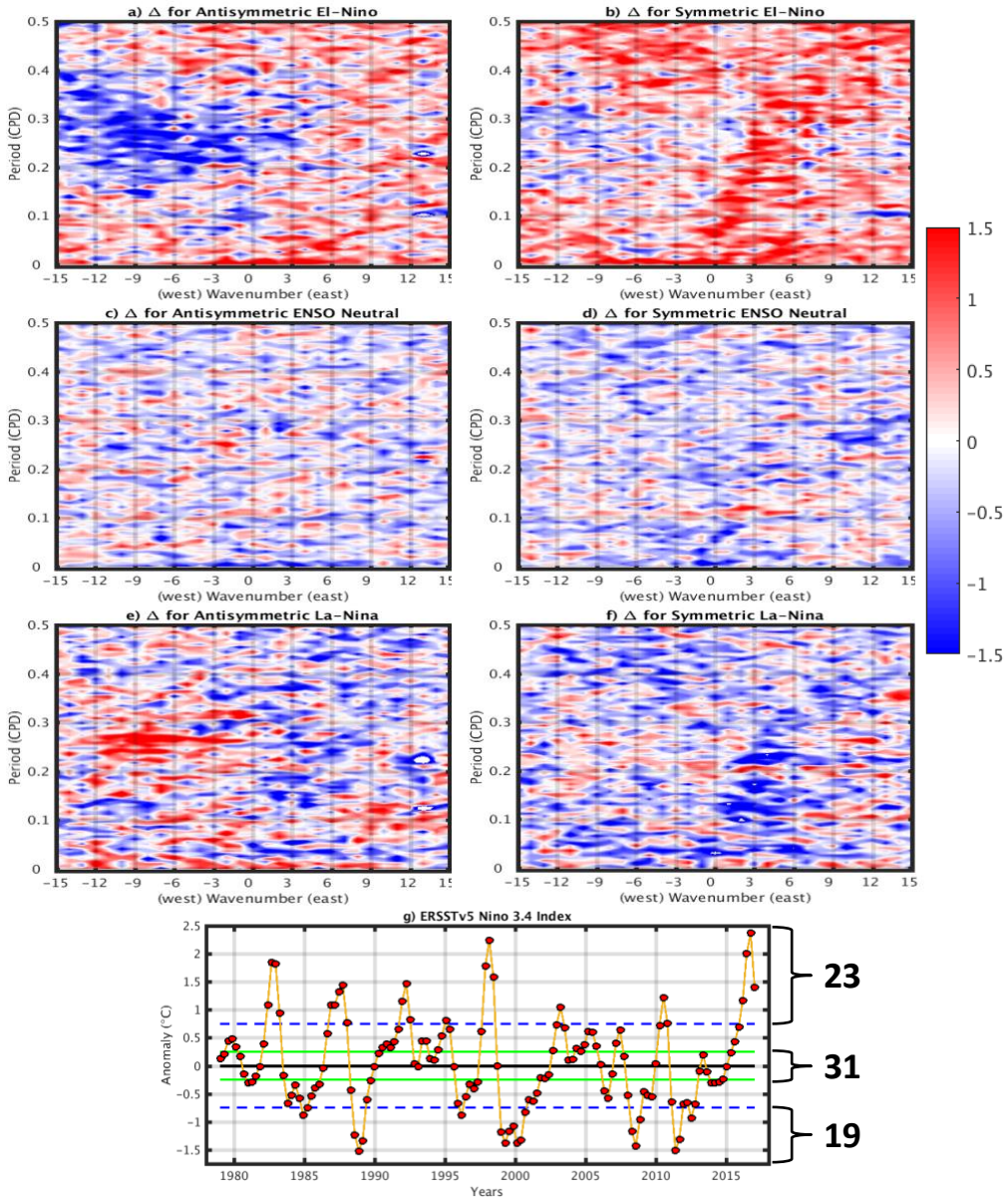

Figure 11: Difference in **P** constructed using NOAA's OLR dataset for each ENSO state for the antisymmetric and symmetric parts of the spectrum (a–f) relative to the mean power spectrum in Fig. 2. A *two-sample t-tests* shows significantly differences at the 1% level between panels a–f. g) The Niño 3.4 index derived from ERSSTv5. The blue and green lines represent the ±0.75 and ±0.25 thresholds used to segregate the time windows to obtain a composite spectrum for a particular ENSO state. The number of time windows in each ENSO state is shown in bold numbers.